

# Thermal conductivity of 3C-SiC from configuration space sampling

Paweł T. Jochym \* and Jan Łażewski 

Institute of Nuclear Physics, Polish Academy of Sciences, Cracow, Poland

\* [pawel.jochym@ifj.edu.pl](mailto:pawel.jochym@ifj.edu.pl)

## Abstract

Cubic silicon carbide phonon thermal conductivity has been calculated using anharmonic phonon analysis. The atomic interaction model was built using displacement-force data obtained with the High Efficiency Configuration Space Sampling (HECSS) technique and density functional theory calculated forces. In the new version of HECSS we replaced the Markov chain scheme of Metropolis-Hastings Monte-Carlo with weighting of the final sampling according to the target distribution. This increased the efficiency of the method and allowed to use – with appropriate weight – all generated and ab-initio evaluated samples. The quality of the proposed method is confirmed by the accuracy with which the experimental results taken from the literature were reproduced.

Copyright attribution to authors.

This work is a submission to SciPost Physics.

License information to appear upon publication.

Publication information to appear upon publication.

Received Date

Accepted Date

Published Date

## Contents

<b>1</b>	<b>Introduction</b>	<b>1</b>
<b>2</b>	<b>Calculation methods</b>	<b>3</b>
2.1	Distribution shaping	3
2.2	Lattice dynamics	4
2.3	Phonon lifetime and lattice thermal conductivity	8
<b>3</b>	<b>Results</b>	<b>8</b>
<b>4</b>	<b>Conclusions</b>	<b>11</b>
	<b>References</b>	<b>11</b>

## 1 Introduction

Silicon Carbide (SiC) can crystallize in the rich family of polytypes. It is quite exceptional, having more than 250 possible structures identified [1–3]. The stoichiometry of all polytypes

is the same (50:50 proportion of Si and C), the only difference is the stacking order and arrangement of consecutive atomic layers. This results in cubic, hexagonal, or rhombohedral structures as well as lower symmetry polytypes with very large lattice vectors (even above 300 nm [2]). Despite this large spectrum of structures, only hexagonal (4H-SiC, 6H-SiC) and cubic (3C-SiC) are commercially available. The structure determines the properties of the material, but since the composition of all polytypes is the same, they all fall in the same ballpark. All structures are classified as wide band gap semiconductors, with a gap energy of 2.3-3.2 eV, which is much higher than silicon. At the same time, they have a large breakdown field (200-400 MV/m). These properties result in low on-state resistance and, simultaneously, low leakage current. Combined with high saturated electron velocity, which is important for high-frequency behavior, and thermal conductivity approximately three times higher than silicon all these properties make silicon carbide a promising material for all kinds of industrial applications, particularly for devices working in high-temperature environments, and potential alternative to currently used semiconductors (e.g. gallium nitride). What is more, SiC is also known to be bio-compatible [4,5] and radiation resistant [6].

The material is not without some drawbacks, the major one being the difficulty of growing large-volumes good-quality single crystals, similarly to silicon monocrystals. Although one can grow 3C-SiC epilayers on silicon wafers investigated and developed starting from the early 1980s [7–13], they are still of relatively low crystallographic quality, which limits their applications and favors more expensive hexagonal bulk SiC wafers in the fabrication of devices requiring larger volume and/or higher crystal quality.

The electrical properties mentioned above make silicon carbide a promising material for the production of high-power, high-temperature devices. The application range is, however, not limited to these fields. The electro-optical properties of this material, including large second-order ( $\chi^2$ ) susceptibility [14] and high third-order non-linearity ( $\chi^3$ ) [15, 16], make it also valuable for optical frequency conversion [17] devices. Particularly, due to its aforementioned favorable properties as well as high chemical resistance [18], hardness ( $E \approx 450$  GPa), and high thermal conductivity [19]. This last property plays a significant role in high-power applications since it helps to quickly remove the dissipated heat from the device using the substrate as a heat conductor instead of elaborated heat transport solutions (e.g. bonded copper heat spreaders which need to be electrically insulated from the device, while being in good thermal contact with the heat-producing active parts).

The ability to accurately predict thermal conductivity for a novel material or structure using *ab-initio* computation has been one of the goals for computational material science. While the theoretical framework of heat transport in crystalline solids is well understood [20, 21], its practical application encounters numerous difficulties. Firstly, heat transport is connected with phonon interactions and energy exchange between vibration modes. Thus, it is an intrinsically *anharmonic* process – since harmonic phonons do not interact. Secondly, the interaction model used to construct lattice dynamics should correspond to a physically realistic state of the system, which is a thermodynamic equilibrium at a given temperature. Thus, we need to build an anharmonic interaction model for the system. Such a model requires a large set of parameters – interatomic force constants (IFCs), which are often obtained from the molecular dynamics [22–24]. This approach, while quite expensive computationally, simultaneously solves the second of the above difficulties by deriving data for the interaction model from the representation of the thermal equilibrium provided by the molecular dynamics. In our work, we have used a similar approach of constructing the interaction model from the representation of the thermal equilibrium state, but we have replaced the molecular dynamics with the recently introduced HECSS method [25] which samples the thermodynamic ensemble with high efficiency. The anharmonic lattice dynamics model is then used to calculate the temperature-dependent heat conduction coefficient for the finite 3C-SiC crystal.

## 2 Calculation methods

The determination of the thermal conductivity of the crystal necessitates the development of an anharmonic lattice dynamics model that corresponds to the thermal equilibrium. Traditionally, this is done with the displacement-force data set generated with *ab-initio* molecular dynamics [23]. This method is computationally expensive and quite wasteful – since one throws away most of the data computed along the trajectory. Instead, we have used the thermodynamic ensemble sampling technique (HECSS) based on the generalized equipartition theorem. The details of the approach are described in our earlier work [25]. This approach was already successfully used to investigate negative thermal expansion [26], structural phase transitions [27, 28], orbital order [29] and chiral phonons [30]. These results demonstrate that it is possible to effectively generate samples providing an appropriate representation of the system in thermal equilibrium at a given temperature and build an adequate lattice dynamics model for the material extending to the analysis of negative thermal expansion effects [26].

Here, we present a series of calculations for the 3C-SiC using VASP as a source of energies and forces, using a range of the system sizes (from  $2^3$  to  $5^3$  supercell) and standard PAW-PBE calculation setup [31–34]. The aim of our work is to calculate phononic thermal conductivity based on anharmonic lattice dynamics derived from the DFT data. This goal requires substantially more data points, comparing to standard lattice dynamics calculation, due to the large number of independent interatomic force constants (IFCs) of the third and fourth order required to derive an anharmonic lattice dynamics model.

The DFT calculations used standard PAW-PBE atomic datasets with energy cut-offs increased by 30% above standard value (i.e. 'Accurate' mode of VASP),  $\Gamma$ -centered k-space sampling grid with a maximum spacing of 0.25 Å and  $\Delta E = 10^{-7}$  eV iteration stopping criterion. The HECSS procedure was used to generate enough data points to obtain 5% convergence of the phonon frequencies derived from the fitted IFCs. The IFC fitting procedure employed ALAMODE [35–38] code to fit the interaction model and calculate lattice dynamics parameters (phonon frequencies and lifetimes) of the investigated crystal.

### 2.1 Distribution shaping

Faithful representation of thermodynamic ensemble for the system in thermal equilibrium requires generating correct sampling of the configurations of the system with correct, Gaussian, energy distribution centered around  $\bar{E} = 3k_B T/2$  (in three dimensions) [25]. This is almost automatically achieved for large systems, thanks to the central limit theorem, but for typical systems used in DFT calculations of tens of atoms must be carefully observed and verified.

The standard HECSS procedure, described in our earlier work [25], generates the energy probability distribution using the standard Metropolis-Hastings algorithm. This algorithm is an established cornerstone of the probability distribution sampling field. However, it requires a large number of samples to achieve high-quality sampling of the distribution. To improve the efficiency of the whole procedure we have developed a simple weighting procedure based on a few observations applicable to energy distribution for systems in thermal equilibrium (but not necessarily to other distributions):

- Any atomic configuration is possible, thus all generated configurations can be included in the sampling;
- The proper representation of thermal equilibrium requires the assignment of appropriate probabilities (weights) to the configurations;
- The Metropolis-Hastings generates the weights by multiplication of samples with the largest probabilities;

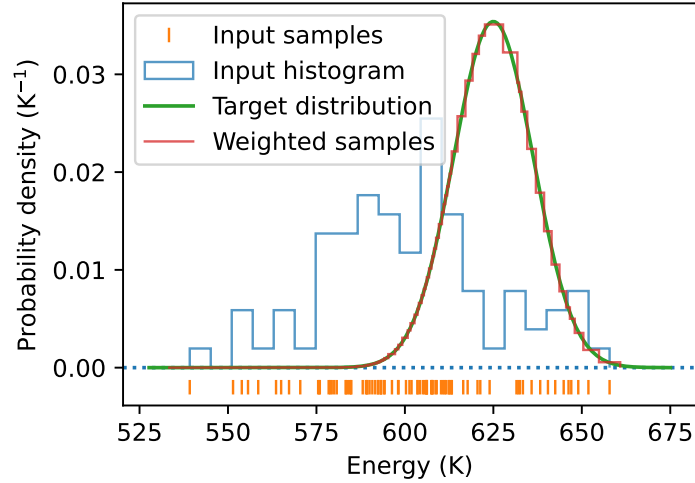


Figure 1: DFT-calculated potential energy distribution generated with HECSS for target temperature  $T = 600$  K reshaped to artificial distribution (green line), centered at 625 K and squeezed by the factor of 2. The resulting step-wise approximation of the target distribution is plotted as a red line. Orange lines at the bottom indicate the energies of the input samples.

- The weights may be calculated directly, provided we know the full formula for the target distribution;
- In the case of thermal equilibrium we know all required parameters (i.e. functional shape, its parameters, and norm).

The resulting sampling may be understood as a step-wise approximation of the target distribution, as illustrated in Figure 1 using actual DFT data from the system of 512 atoms ( $4 \times 4 \times 4$  supercell) at 600 K and artificial target distribution which is, for illustration purposes, shifted by 25 K and squeezed by the factor of 2 in energy.

The result of this procedure is a substantial increase in the effectiveness of the distribution sampling and improved elasticity of the whole procedure. The main benefits are:

- All data points are used in the final sampling with weights adjusted according to the target distribution;
- It is possible to change the parameters of the final distribution without re-calculating of any input (DFT) data points;
- When the input data set spans a range of energies, it is possible to generate samplings for any temperature corresponding to the whole energy range (i.e. scan the temperature range) without any recalculation of DFT input data.

## 2.2 Lattice dynamics

Since the described method is a modification of the original HECSS procedure [25], we need to check if the convergence properties still hold true. The final distribution is properly generated in the new procedure by construction. Thus, we have decided to use the lattice dynamics, derived from the model constructed based on the generated sampling, as a validity check for the new procedure. We have selected RMS difference between frequencies evaluated on the

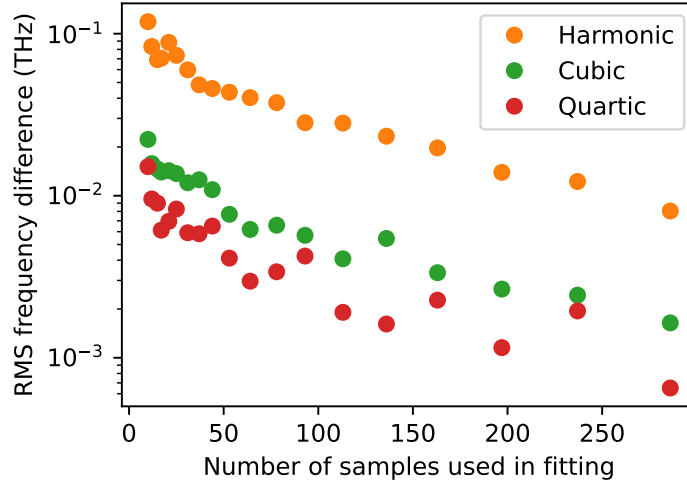


Figure 2: Convergence of phonon frequencies with respect to the number of samples. The samples were randomly selected from the full set of weighted samples from the full HECSS procedure.

$20 \times 20 \times 20$  grid with models derived from the varying number of samples — randomly selected from the whole sampling — against the frequencies calculated from the full set of samples.

The results of this comparison executed for harmonic, cubic, and quartic models are presented in Figure 2. The difference between harmonic and non-harmonic models is clearly visible there. The harmonic model, which is the simplest approximation shows the strongest dependence on the number of samples, while anharmonic models — probably better fitting the interaction potential show much smaller variability. This effect appears despite a much smaller number of parameters of the harmonic model in comparison with cubic or quartic models.

The comparison of RMS residuals from the models presented in Figure 3 further confirms the above conclusion and directly shows significantly smaller residuals of the higher-order models, i.e. a much better representation of the input data by the anharmonic models (cubic and quartic). The linear, in the log-log graph, character of the RMS curves in Figure 3 should be attributed to the statistical reasons. It is only expected that the standard deviation of the random variable falls inversely proportionally to the square root of the number of samples  $\sqrt{N}$  (dotted line in Figure 3). Thus, this aspect of the data is not specific to the presented case. On the other hand, the relative quality of the models is represented by the relationship between their trend lines - showing well over one order of magnitude difference between harmonic and quartic models and indicating non-negligible anharmonic component in the data.

The standard procedure for extraction of the interatomic force constants (IFC) involves fitting of the parameters of the model potential to the displacement-force data provided by the HECSS procedure described above. The shape of the model potential is defined by its order - in this work we have used a fourth-order potential which corresponds to four body interactions in the system. The form of the potential is further determined by the range of the interactions (two-, three-, and four-body) specified by the cutoff distances, separately for each order of interaction and type of interaction (e.g. C-C, C-Si, etc.). The implementation of the TDEP scheme (ALAMODE [35–38]) used in this work provides great flexibility in this regard. The quality of the fit strongly depends on the selection of the order and cutoff radii for the interaction model. Unfortunately, the computational cost of the fitting procedure grows very fast with the expansion of the cutoffs, due to very fast growth of the parameter space of the potential. For the 8 and 6 Å cutoffs, for third and fourth-order IFCs respectively, the number of free parameters exceeds 30 000.

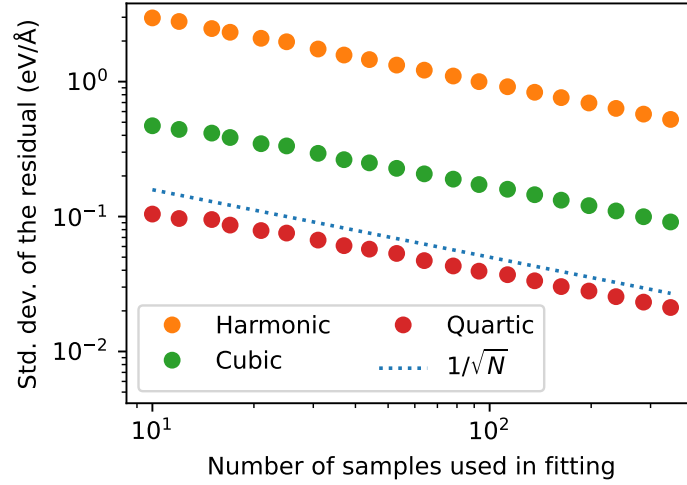


Figure 3: Standard deviation of the residual of the models with respect to number of used samples. The samples were randomly selected from the full set of weighted samples from the full HECSS procedure. The dotted line represents a function proportional to  $1/\sqrt{N}$ , where  $N$  is the number of samples used in the fit.

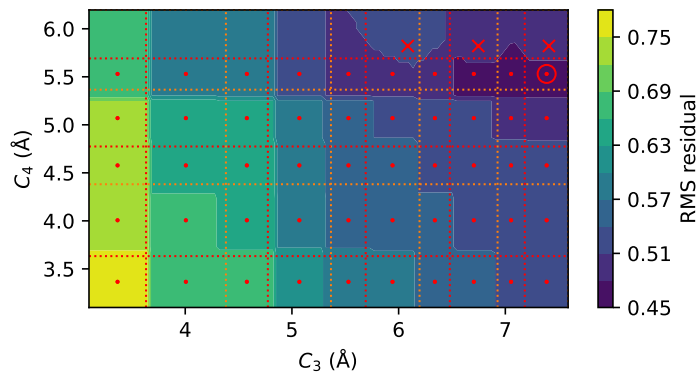


Figure 4: Relative RMS fitting errors as a function of three- and four-body cutoffs used in the fitting procedure. Red dots mark a combination of cutoffs used in test runs, the color map is a nearest neighbor interpolation of data obtained at those points. Red x's mark calculations with expanded C-Si interaction range. The selected combination of cutoffs is marked with an open red circle. Red and orange dotted lines mark distances of consecutive coordination shells in the structure: C-Si (red) and C-C, Si-Si (orange). See also description in the text.

To select optimal set of cutoffs providing high accuracy we have executed a series of test calculations on 900 K dataset with various parameters. Summary of these calculations is presented in Figure 4 as a map of the fit residuals produced by the third- and fourth-order cutoffs ( $C_3$  and  $C_4$  respectively). Considering the important role anharmonic interactions play in thermal conductivity phenomena we have selected cutoffs of 7.5 and 5.5 Å for third and fourth-order IFCs, respectively. The selected parameters are marked with an open circle in Figure 4. The selection was guided by the quality of the obtained models and positions of the coordination spheres in the system (red/orange dotted lines in Figure 4) and led to the 19 000 IFCs in the used interaction model. The quality of constructed model is indicated by the value of residuals, which are 0.46 for the full anharmonic model, relative to 11.36 for the harmonic model.

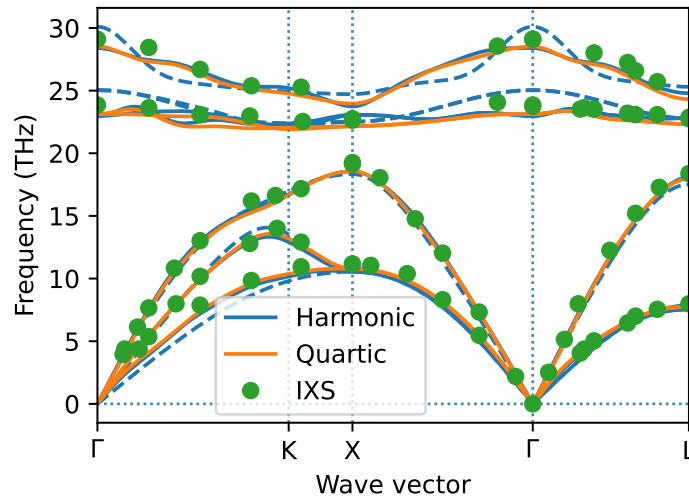


Figure 5: Phonon dispersion relation calculated with harmonic (solid and dashed blue line) and quartic models (orange solid line) compared to experimental data from inelastic X-ray scattering [39]. The dashed blue line shows the harmonic model derived using interaction cutoff  $C_2 = 3.7$  Å.

The vibrational modes in the system depicted in Figure 5 were calculated from the IFCs of the model with standard dynamical matrix diagonalization implemented in ALAMODE package. The Born effective charges, required for non-analytical term correction, were taken from the measurements of Olego, Cardona, and Vogl [40].

The contrast between the quality of harmonic and anharmonic models suggests the important role of anharmonicity in the description of the system. Furthermore, substantial change in the fits' residuals along  $C_4$  axis in Figure 4 indicate a non-negligible role of fourth-order anharmonicity. However, as is clearly visible in Figure 5 its influence on lattice vibrations is small and limited mostly to optical branches near X point in the Brillouin zone.

The comparison with experimental data obtained with inelastic x-ray scattering [39] and included in Figure 5 (green dots) demonstrates that even the harmonic model (blue line) fits well with experimental frequencies if the interaction range is large enough. The effects of shortening of the interaction range are demonstrated by the dashed blue line in Figure 5 calculated with harmonic interaction cutoff reduced to  $C_2 = 3.7$  Å.

Small differences in frequency terms between harmonic and quartic models visible in Figure 5 indicate a small influence of the fourth-order anharmonicity on the vibrational frequencies in this material. To verify this conclusion we have performed a series of self-consistent phonon (SCPH) calculations using the final, best-fit model for the temperatures between 200 K

and 1200 K. The maximum RMS difference between renormalized SCPH frequencies at extreme temperatures turned out to be consistent with zero ( $\approx 0.1 \pm 0.1$  THz), validating the above conclusion. Thus, the only remaining significant anharmonic part of the model is the cubic term, which mainly influences the lifetimes of the phonons in the system.

### 2.3 Phonon lifetime and lattice thermal conductivity

The goal of this work is calculation of the lattice contribution to the thermal conductivity of the 3C-SiC crystal. We have estimated lattice thermal conductivity tensor, using relaxation time approximation [20, 37, 41], as:

$$\kappa_{\text{ph}}^{\mu\nu}(T) = \frac{1}{VN} \sum_{\mathbf{q},j} c_{\mathbf{q}j}(T) v_{\mathbf{q}j}^{\mu} v_{\mathbf{q}j}^{\nu} \tau_{\mathbf{q}j}(T), \quad (1)$$

where  $\tau_{\mathbf{q}j}(T)$  is a  $j$ -th branch phonon lifetime at point  $\mathbf{q}$  in the reciprocal space and temperature  $T$ . Mode group velocities  $\mathbf{v}_{\mathbf{q}j} = \frac{\partial \omega_{\mathbf{q}j}}{\partial \mathbf{q}}$  are evaluated in ALAMODE by central difference formula. Finally,  $V$  is the unit cell volume,  $N$  is the number of unit cells in the crystal and mode heat capacity is  $c_{\mathbf{q}j} = \hbar \omega_{\mathbf{q}j} \partial n_{\mathbf{q}j} / \partial T$ , where mode energy is proportional to its frequency  $\omega_{\mathbf{q}j}$  and Bose-Einstein distribution  $n_{\mathbf{q}j} = 1 / (e^{\hbar \omega_{\mathbf{q}j} / kT} - 1)$ .

Phonon lifetime  $\tau_{\mathbf{q}j}(T)$  is derived from mode linewidths connected with anharmonic interactions  $\Gamma_{\mathbf{q}j}^{\text{anh}}$ , and isotope scattering  $\Gamma_{\mathbf{q}j}^{\text{iso}}$  with Matthiessen's formula:

$$\tau_{\mathbf{q}j}^{-1}(T) = 2 \left( \Gamma_{\mathbf{q}j}^{\text{anh}}(T) + \Gamma_{\mathbf{q}j}^{\text{iso}} \right). \quad (2)$$

The components of the phonon linewidth in the above equation are anharmonic processes, mainly third-order components of the interaction model [35, 37, 38] and isotope scattering included following the mass perturbation approach [42].

The results presented above indicate a rather quick convergence of the harmonic model with the size of the sample and interaction cutoff. This is not very surprising, due to the relatively small size of the parameter set and close to linear relationship between displacements and forces acting on atoms in the 3C-SiC crystal. In contrast, a higher-order model cannot benefit from such circumstances, since it requires a large number of parameters (orders of magnitude higher than harmonic case) which are determined by higher derivatives of the energy surface. Thus, it is only expected that quantities such as phonon lifetimes or thermal conductivity of the material may be much more sensitive to subtle features of the sampling used and require larger samples to converge [25].

## 3 Results

As described above, the thermal conductivity is necessarily connected with phonon-phonon and phonon-lattice interaction. The first phenomenon facilitates the distribution of energy over all degrees of freedom, the second mainly dissipates phonon energy (e.g. defect scattering, including isotopic mass defects) or transports energy to the different parts of the Brillouin zone (e.g. umklapp processes and boundary reflection/scattering). Both kinds of processes constitute a deviation from the strictly harmonic regime (i.e. non-interacting phonons) and require either third-order contributions to the interaction potential or separate modeling (e.g. Matthiessen's formula used for isotope scattering). The third-order interactions are usually a leading contribution to phonon lifetimes. The next, fourth order, the term is responsible for shifting the phonon frequencies - since it mainly modifies the curvature of the energy surface. As is obvious from Fig. 5 and the SCPH calculations reported above, the shifts due to the

quartic (fourth-order) components of the interaction potential are very small and limited to the fine parts of the optical spectra near the X point.

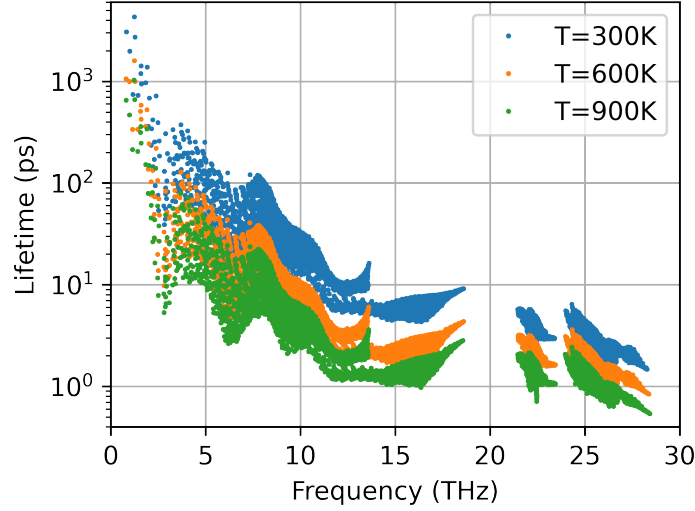


Figure 6: Phonon lifetimes calculated with RTA at  $T = 300, 600, 900$  K, from the fourth-order potential model fitted to HECSS samples corresponding to the same temperature. Temperatures marked with colors (300 K – blue, 600 K – orange, and 900 K – green).

The influence of the third-order terms is more pronounced. The phonon lifetimes calculated with Boltzmann transport equation and Relaxation Time Approximation (BTE/RTA) plotted in Figure 6 as a function of frequency for three different temperatures show a quite strong temperature dependence and fairly short lifetimes (below 1 ps for the top of the spectrum and high temperatures). This indicates substantial third-order anharmonicity in the system.

The phonon lifetime is not very easy to measure. This is just the first step to determining the ultimate goal of our work, which is the thermal conductivity coefficient for the material. The lattice thermal conductivity  $\kappa$  is a sum of frequency-dependent terms also weighted by the Boltzmann factor. Thus proper sampling of the reciprocal space and energy scale is crucial for obtaining good accuracy of the final result. The spectral decomposition of the thermal conductivity contributions presented in Fig. 7 clearly shows that the selection of too coarse a grid for the calculation of the phonon lifetimes removes low-frequency parts from the sum and may strongly influence the final result. The data in Fig. 7 indicates that the  $30 \times 30 \times 30$  points grid may already be dense enough. For the final results, we have selected a slightly denser grid of  $40 \times 40 \times 40$  points. On the other hand, the comparison between two levels of the interaction model (cubic – dashed line and quartic – solid line), indicates a much smaller influence of this aspect. However, the quartic model seems to be more stable between different grid spacings. Thus, the quartic model was selected for the final calculation.

The Peierls term (1) contains contributions from all wavelengths possible in the infinite crystal. This sum at low temperatures is dominated by the contributions from the acoustic modes with very low frequencies and high Boltzmann factor and exhibits infrared divergency common in such cases. This, obviously non-physical effect is shown in Figure 8 by the dotted line. The realistic calculation of the thermal conductivity of the material requires inclusion of several finite-scale effects present in the real crystal: isotope defect scattering, lattice defects scattering, and finite crystallite size effects. The isotope scattering influence, in the case of 3C-SiC, is vanishingly small (below  $10^{-3}$ ). The lattice defects play a much larger role but their influence is strongly sample-dependent and difficult to estimate. The final crystal size,

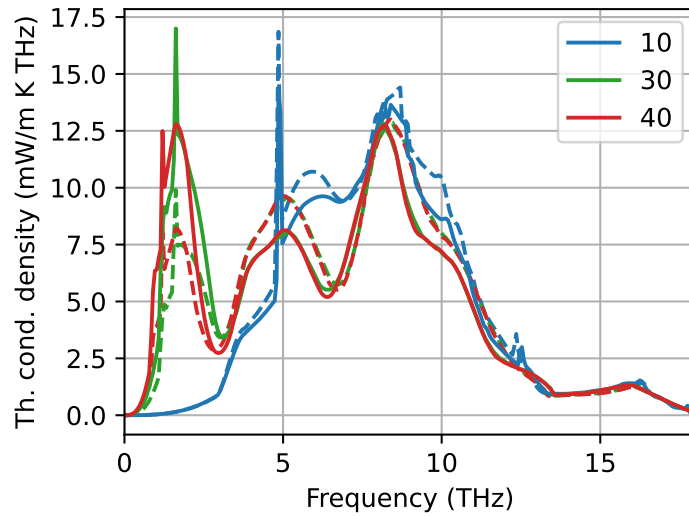


Figure 7: Thermal conductivity spectral density for different k-grid sizes for the RTA procedure ( $10^3$ ,  $30^3$ ,  $40^3$  respectively) and interaction model order (cubic - dashed line, quartic - solid line).

on the other hand, has a major influence on thermal conductivity and is quite easy to include in the calculation — by simply limiting the wavelengths of the contributions to the size of the crystal.

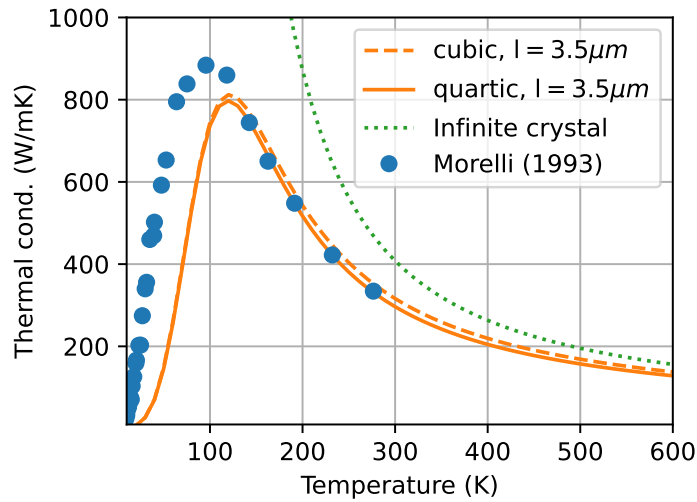


Figure 8: Thermal conductivity coefficient calculated from samples generated with temperatures  $T = 900$  K and k-grid size  $40 \times 40 \times 40$  in RTA calculation. The conductivity is calculated for the  $3.5 \mu\text{m}$  grain size. The full line represents the quartic interaction model, the dashed line cubic interaction model. The dotted line represents the result for the infinite crystal. The laboratory measurements (full dots) are from [43].

The  $\kappa(T)$  curve plotted in Fig 8 was calculated with the assumption of average crystal size of  $L = 3.5 \mu\text{m}$ . The comparison with experimental data from [43] shows remarkably good agreement with the measurements above 120 K. The low-temperature discrepancy can be attributed to scattering on lattice imperfections — as they influence the curve similarly as

the finite size of the crystal. Furthermore, a strong influence of defects should be expected due to the known difficulty of growing 3C-SiC monocrystals. Unfortunately, the experimental data contains no information about the grain size or defect concentration in the sample.

As we mentioned discussing Fig 7, the degree of the interaction model plays rather a minor role in this type of calculation. This is confirmed by the insignificant difference between results from the cubic model (dashed line in Fig 8) and the quartic one (solid line).

## 4 Conclusions

The results presented above demonstrate potential of the proposed HECSS approach to generate a faithful representation of the system in thermal equilibrium at elevated temperatures with only a very small number of rejected DFT calculations – thus very high efficiency. The proposed new method of evaluation of sample weights further improved the effectiveness of the original HECSS approach [25] and added the ability to shift the target temperature within the sampled energy range. The data from such samplings allowed construct the high-accuracy anharmonic (quartic) interaction model and calculate lattice thermal conductivity of 3C-SiC which closely matches experimental data above  $T=120$  K. The extension of the results to lower temperatures is limited only by further post-processing of data from the interaction model to include lattice imperfection and finite-size effects which play an important role in low-temperature thermal transport.

## Acknowledgements

The authors would like to express their gratitude to Krzysztof Parlinski, Przemysław Piekarz, Andrzej M. Oleś, and Małgorzata Sternik for inspiring and fruitful discussions. This work was partially supported by the National Science Centre (NCN, Poland) under grant UMO-2014/13/B/ST3/04393.

## References

- [1] R. Cheung, ed., *Silicon Carbide Microelectromechanical Systems for Harsh Environments*, Imperial College Press, London, ISBN 978-1-86094-624-0 (2006).
- [2] J. F. Kelly, G. R. Fisher and P. Barnes, *Correlation between layer thickness and periodicity of long polytypes in silicon carbide*, *Materials Research Bulletin* **40**(2), 249 (2005), doi:[10.1016/j.materresbull.2004.10.008](https://doi.org/10.1016/j.materresbull.2004.10.008).
- [3] T. L. Daulton, T. J. Bernatowicz, R. S. Lewis, S. Messenger, F. J. Stadermann and S. Amari, *Polytype Distribution in Circumstellar Silicon Carbide*, *Science* **296**(5574), 1852 (2002), doi:[10.1126/science.1071136](https://doi.org/10.1126/science.1071136).
- [4] S. E. Saddow, *Silicon Carbide Biotechnology: A Biocompatible Semiconductor for Advanced Biomedical Devices and Applications*, Elsevier (2011).
- [5] S. E. Saddow, C. Frewin, M. Reyes, J. Register, M. Nezafati and S. Thomas, *3C-SiC on Si: A Biocompatible Material for Advanced Bioelectronic Devices*, *ECS Trans.* **61**(7), 101 (2014), doi:[10.1149/06107.0101ecst](https://doi.org/10.1149/06107.0101ecst).

- [6] F. Nava, E. Vittone, P. Vanni, G. Verzellesi, P. Fuochi, C. Lanzieri and M. Glaser, *Radiation tolerance of epitaxial silicon carbide detectors for electrons, protons and gamma-rays*, Nuclear Instruments and Methods in Physics Research Section A: Accelerators, Spectrometers, Detectors and Associated Equipment **505**(3), 645 (2003), doi:[10.1016/S0168-9002\(02\)01558-9](https://doi.org/10.1016/S0168-9002(02)01558-9).
- [7] A. Severino, C. Bongiorno, N. Piluso, M. Italia, M. Camarda, M. Mauceri, G. Condorelli, M. A. Di Stefano, B. Cafra, A. La Magna and F. La Via, *High-quality 6inch (111) 3C-SiC films grown on off-axis (111) Si substrates*, Thin Solid Films **518**(6, Supplement 1), S165 (2010), doi:[10.1016/j.tsf.2009.10.080](https://doi.org/10.1016/j.tsf.2009.10.080).
- [8] S. Nishino, J. A. Powell and H. A. Will, *Production of large-area single-crystal wafers of cubic SiC for semiconductor devices*, Applied Physics Letters **42**(5), 460 (1983), doi:[10.1063/1.93970](https://doi.org/10.1063/1.93970).
- [9] S. Nishino, H. Suhara, H. Ono and H. Matsunami, *Epitaxial growth and electric characteristics of cubic SiC on silicon*, Journal of Applied Physics **61**(10), 4889 (1987), doi:[10.1063/1.338355](https://doi.org/10.1063/1.338355).
- [10] P. Liaw and R. F. Davis, *Epitaxial Growth and Characterization of  $\beta$  - SiC Thin Films*, J. Electrochem. Soc. **132**(3), 642 (1985), doi:[10.1149/1.2113921](https://doi.org/10.1149/1.2113921).
- [11] A. J. Steckl and J. P. Li, *Epitaxial growth of beta-SiC on Si by RTCVD with C<sub>3</sub>H<sub>8</sub> and SiH<sub>4</sub>*, IEEE Transactions on Electron Devices **39**, 64 (1992), doi:[10.1109/16.108213](https://doi.org/10.1109/16.108213).
- [12] N. Nordell, A. Schöner and S. G. Andersson, *Design and Performance of a New Reactor for Vapor Phase Epitaxy of 3C, 6H, and 4H SiC*, J. Electrochem. Soc. **143**(9), 2910 (1996), doi:[10.1149/1.1837126](https://doi.org/10.1149/1.1837126).
- [13] O. Kordina, L.-O. Björketun, A. Henry, C. Hallin, R. Glass, L. Hultman, J.-E. Sundgren and E. Janzén, *Growth of 3C-SiC on on-axis Si(100) substrates by chemical vapor deposition*, Journal of Crystal Growth **154**(3-4), 303 (1995), doi:[10.1016/0022-0248\(95\)00136-0](https://doi.org/10.1016/0022-0248(95)00136-0).
- [14] I. J. Wu and G. Y. Guo, *Second-harmonic generation and linear electro-optical coefficients of SiC polytypes and nanotubes*, Phys. Rev. B **78**(3), 035447 (2008), doi:[10.1103/PhysRevB.78.035447](https://doi.org/10.1103/PhysRevB.78.035447).
- [15] J. Cardenas, M. Yu, Y. Okawachi, C. B. Poitras, R. K. W. Lau, A. Dutt, A. L. Gaeta and M. Lipson, *Optical nonlinearities in high-confinement silicon carbide waveguides*, Opt. Lett., OL **40**(17), 4138 (2015), doi:[10.1364/OL.40.004138](https://doi.org/10.1364/OL.40.004138).
- [16] F. Martini and A. Politi, *Four wave mixing in 3C SiC ring resonators*, Applied Physics Letters **112**(25), 251110 (2018), doi:[10.1063/1.5034456](https://doi.org/10.1063/1.5034456).
- [17] D. M. Lukin, C. Dory, M. A. Guidry, K. Y. Yang, S. D. Mishra, R. Trivedi, M. Radulaski, S. Sun, D. Verduyck, G. H. Ahn and J. Vučković, *4H-silicon-carbide-on-insulator for integrated quantum and nonlinear photonics*, Nat. Photonics **14**(5), 330 (2020), doi:[10.1038/s41566-019-0556-6](https://doi.org/10.1038/s41566-019-0556-6).
- [18] W. Daves, A. Krauss, N. Behnel, V. Häublein, A. Bauer and L. Frey, *Amorphous silicon carbide thin films (a-SiC:H) deposited by plasma-enhanced chemical vapor deposition as protective coatings for harsh environment applications*, Thin Solid Films **519**(18), 5892 (2011), doi:[10.1016/j.tsf.2011.02.089](https://doi.org/10.1016/j.tsf.2011.02.089).

- [19] K. Jackson, J. Dunning, C. Zorman, M. Mehregany and W. Sharpe, *Mechanical properties of epitaxial 3C silicon carbide thin films*, Journal of Microelectromechanical Systems **14**(4), 664 (2005), doi:[10.1109/JMEMS.2005.847933](https://doi.org/10.1109/JMEMS.2005.847933).
- [20] R. Peierls, *Zur kinetischen Theorie der Wärmeleitung in Kristallen*, Annalen der Physik **395**(8), 1055 (1929), doi:[10.1002/andp.19293950803](https://doi.org/10.1002/andp.19293950803).
- [21] M. Simoncelli, N. Marzari and F. Mauri, *Unified theory of thermal transport in crystals and glasses*, Nat. Phys. **15**(8), 809 (2019), doi:[10.1038/s41567-019-0520-x](https://doi.org/10.1038/s41567-019-0520-x).
- [22] O. Hellman, I. A. Abrikosov and S. I. Simak, *Lattice dynamics of anharmonic solids from first principles*, Phys. Rev. B **84**(18), 180301 (2011), doi:[10/cp7gkg](https://doi.org/10/cp7gkg).
- [23] O. Hellman, P. Steneteg, I. A. Abrikosov and S. I. Simak, *Temperature dependent effective potential method for accurate free energy calculations of solids*, Phys. Rev. B **87**(10), 104111 (2013), doi:[10/f2z3ds](https://doi.org/10/f2z3ds).
- [24] O. Hellman and I. A. Abrikosov, *Temperature-dependent effective third-order interatomic force constants from first principles*, Phys. Rev. B **88**(14), 144301 (2013), doi:[10/f24fvq](https://doi.org/10/f24fvq).
- [25] P. Jochym and J. Łazewski, *High Efficiency Configuration Space Sampling – probing the distribution of available states*, SciPost Phys. **10**(6), 129 (2021), doi:[10.21468/SciPostPhys.10.6.129](https://doi.org/10.21468/SciPostPhys.10.6.129).
- [26] P. T. Jochym, R. K. Kremer, J. Łazewski, A. Ptok, P. Piekarz, E. Brücher and A. M. Oleś, *Influence of anharmonicity on the negative thermal expansion of  $\alpha$ -Sn*, Phys. Rev. Materials **6**(11), 113601 (2022), doi:[10.1103/PhysRevMaterials.6.113601](https://doi.org/10.1103/PhysRevMaterials.6.113601).
- [27] A. Ptok, A. Kobiałka, M. Sternik, J. Łazewski, P. T. Jochym, A. M. Oleś and P. Piekarz, *Dynamical study of the origin of the charge density wave in  $AV_3Sb_5$  ( $A = K, Rb, Cs$ ) compounds*, Phys. Rev. B **105**(23), 235134 (2022), doi:[10.1103/PhysRevB.105.235134](https://doi.org/10.1103/PhysRevB.105.235134).
- [28] S. Pastukh, P. T. Jochym, O. Pastukh, J. Łazewski, D. Legut and P. Piekarz, *Anharmonicity and structural phase transition in the Mott insulator  $Cu_2P_2O_7$* , Phys. Rev. B **108**(10), 104104 (2023), doi:[10.1103/PhysRevB.108.104104](https://doi.org/10.1103/PhysRevB.108.104104).
- [29] A. Ptok, K. J. Kapcia, P. T. Jochym, J. Łazewski, A. M. Oleś and P. Piekarz, *Electronic and dynamical properties of  $CeRh_2As_2$ : Role of  $Rh_2As_2$  layers and expected orbital order*, Phys. Rev. B **104**(4), L041109 (2021), doi:[10.1103/PhysRevB.104.L041109](https://doi.org/10.1103/PhysRevB.104.L041109).
- [30] A. Ptok, A. Kobiałka, M. Sternik, J. Łazewski, P. T. Jochym, A. M. Oleś, S. Stankov and P. Piekarz, *Chiral phonons in the honeycomb sublattice of layered CoSn-like compounds*, Phys. Rev. B **104**(5), 054305 (2021), doi:[10.1103/PhysRevB.104.054305](https://doi.org/10.1103/PhysRevB.104.054305).
- [31] G. Kresse and J. Hafner, *Ab initio molecular-dynamics simulation of the liquid-metal–amorphous-semiconductor transition in germanium*, Physical Review B **49**(20), 14251 (1994), doi:[10/c3qkmv](https://doi.org/10/c3qkmv).
- [32] G. Kresse and J. Furthmüller, *Efficiency of ab-initio total energy calculations for metals and semiconductors using a plane-wave basis set*, Computational Materials Science **6**(1), 15 (1996), doi:[10/bkcfzj](https://doi.org/10/bkcfzj).
- [33] G. Kresse and J. Furthmüller, *Efficient iterative schemes for ab initio total-energy calculations using a plane-wave basis set*, Phys. Rev. B **54**(16), 11169 (1996), doi:[10/fmrkzs](https://doi.org/10/fmrkzs).

- [34] J. P. Perdew, K. Burke and M. Ernzerhof, *Generalized Gradient Approximation Made Simple*, Phys. Rev. Lett. **77**(18), 3865 (1996), doi:[10/bppfwf](https://doi.org/10/bppfwf).
- [35] T. Tadano, Y. Gohda and S. Tsuneyuki, *Anharmonic force constants extracted from first-principles molecular dynamics: Applications to heat transfer simulations*, Journal of Physics: Condensed Matter **26**(22), 225402 (2014), doi:[10/ghwtfz](https://doi.org/10/ghwtfz).
- [36] T. Tadano and S. Tsuneyuki, *Self-consistent phonon calculations of lattice dynamical properties in cubic SrTiO<sub>3</sub> with first-principles anharmonic force constants*, Phys. Rev. B **92**(5), 054301 (2015), doi:[10.1103/PhysRevB.92.054301](https://doi.org/10.1103/PhysRevB.92.054301).
- [37] T. Tadano and S. Tsuneyuki, *First-Principles Lattice Dynamics Method for Strongly Anharmonic Crystals*, J. Phys. Soc. Jpn. **87**(4), 041015 (2018), doi:[10/gc4cc2](https://doi.org/10/gc4cc2).
- [38] Y. Oba, T. Tadano, R. Akashi and S. Tsuneyuki, *First-principles study of phonon anharmonicity and negative thermal expansion in ScF<sub>3</sub>*, Phys. Rev. Materials **3**(3), 033601 (2019), doi:[10.1103/PhysRevMaterials.3.033601](https://doi.org/10.1103/PhysRevMaterials.3.033601).
- [39] J. Serrano, J. Strempler, M. Cardona, M. Schwoerer-Böhning, H. Requardt, M. Lorenzen, B. Stojetz, P. Pavone and W. J. Choyke, *Determination of the phonon dispersion of zinc blende (3C) silicon carbide by inelastic x-ray scattering*, Applied Physics Letters **80**(23), 4360 (2002), doi:[10/d65tgd](https://doi.org/10/d65tgd).
- [40] D. Olego, M. Cardona and P. Vogl, *Pressure dependence of the optical phonons and transverse effective charge in 3C-SiC*, Phys. Rev. B **25**(6), 3878 (1982), doi:[10.1103/PhysRevB.25.3878](https://doi.org/10.1103/PhysRevB.25.3878).
- [41] T. Sun and P. B. Allen, *Lattice thermal conductivity: Computations and theory of the high-temperature breakdown of the phonon-gas model*, Phys. Rev. B **82**(22), 224305 (2010), doi:[10.1103/PhysRevB.82.224305](https://doi.org/10.1103/PhysRevB.82.224305).
- [42] S.-i. Tamura, *Isotope scattering of dispersive phonons in Ge*, Phys. Rev. B **27**(2), 858 (1983), doi:[10.1103/PhysRevB.27.858](https://doi.org/10.1103/PhysRevB.27.858).
- [43] D. T. Morelli, J. Hermans, C. Beetz, W. S. Woo, G. L. Harris and C. Taylor, *Carrier concentration dependence of the thermal conductivity of silicon carbide*, In *Silicon Carbide and Related Materials*, vol. 137 of *IoP Conf. Ser.*, pp. 313–316. Institute of Physics Publishing (1993).